THESIS FOR THE DEGREE OF LICENTIATE OF ENGINEERING

Computational investigation of interface structure and composition in cemented carbides at finite temperatures

Erik Fransson

Department of Physics
CHALMERS UNIVERSITY OF TECHNOLOGY
Göteborg, Sweden 2019

Computational investigation of interface structure and composition in cemented carbides at finite temperatures
Erik Fransson

Department of Physics
Chalmers University of Technology
se-412 96 Göteborg, Sweden
Telephone +46 31 772 10 00

Cover: 3D-rendering of the atomic structure of a cubic thin film at the phase-boundary between WC and Co.

Chalmers reproservice
Göteborg, Sweden 2019

Computational investigation of interface structure and composition in cemented carbides at finite temperatures

Erik Fransson
Department of Physics
Chalmers University of Technology

Abstract

WC-Co cemented carbides combine superb hardness with high toughness making them ideal for usage in high-speed machining of steels and in wear resistance tools. These excellent mechanical properties are to a large extent dependent on the microstructure and thus the interfacial properties of the material. Hence, being able to predict and understand interfacial properties in this material can allow for e.g. optimizing the manufacturing process in order to improve mechanical properties further.

Atomic scale ab-initio calculations allow for accurately predicting interface energies for a given structure and composition. However, finding the ground-state interfacial structure and composition becomes a challenge as the search space is very large when considering all degrees of freedom. Furthermore, direct sampling of interfacial properties at finite temperature using density functional theory (DFT) often becomes computationally unfeasible as hundreds, thousands or even millions of calculations may be required. Therefore, employing atomic scale models based on DFT calculations is advantageous and allows for investigation of the interface structure, composition and free energy at finite temperatures. In this thesis the computational methods for calculating temperature dependent interfacial free energies are developed and applied to the WC-Co system.

An interfacial phase diagram for cubic thin films in undoped WC-Co is constructed. Here, configurational degrees of freedom are treated using cluster expansion models and Monte Carlo sampling. Vibrations are treated in the harmonic approximation using force constant fitting to significantly reduce the number of DFT calculations.

The temperature dependence of interface free energies for surfaces, grain boundaries and phase boundaries is using an analytic bond order potential. Here, multiple different free energy calculation methods are employed such as quasi-harmonic approximation, λ-integration, thermodynamic integration and surface tension calculation.

Keywords: Cemented carbides, Hard Metals, Interfacial free energies, Force constants, Molecular dynamics, Cluster expansion, Monte Carlo

LIST OF PUBLICATIONS

This thesis is based on the work presented in the following papers:

I **A computational study of thin films in WC-Co cemented carbides: Vacancies and vibrations**
Erik Fransson, Martin Gren and Göran Wahnström
In manuscript

II **A computational study of the temperature dependence of interface energies in WC–Co cemented carbides**
Martin Gren, Erik Fransson and Göran Wahnström
In manuscript

III **icet - A Python library for constructing and sampling alloy cluster expansions**
Mattias Ångqvist, William A. Muñoz, J. Magnus Rahm, Erik Fransson, Céline Durniak, Piotr Rozyczko, Thomas Holm Rod, Paul Erhart
Advanced Theory and Simulations 1900015 (2019)

IV **The Hiphive Package for the Extraction of High-Order Force Constants by Machine Learning**
Fredrik Eriksson, Erik Fransson and Paul Erhart
Advanced Theory and Simulations 1800184 (2019)

V **Efficient construction and applications of higher-order force constant models**
Erik Fransson, Fredrik Eriksson and Paul Erhart
In manuscript, preprint available at arXiv:1902.01271

Specification of the authors contribution to the publications:

I The author wrote the paper and did the atomistic modeling of the free energy. The author did not carry out the DFT calculations.

II The author carried out the free energy calculations besides the ones concerning the solid-liquid interfaces.

III The author helped with training of the cluster-expansions for the Ag-Pd application. The author developed the fitting module for icet.

IV The author was part of developing hiphive. The author also did the fourth order nickel analysis in the paper.

V The author carried out most the analysis for the applications and wrote the first draft of the paper (excluding introduction).

Contents

1

Atomic-scale computational materials science

On of the more popular computational methods for solving the many-body quantum mechanical problem for electrons in condensed matter or chemistry is density functional theory (DFT). DFT is a first principle method, i.e. no extra parameters are apart from the atomic positions and numbers are needed to carry out calculations of electronic properties. It does, however, require an approximate description of the exchange correlation function. DFT has been used through out the years with great success. The quick advances in both computational power and algorithms have allowed for using electronic structure calculations to predict various characteristics of materials. Fundamental understanding of materials has been improved and new materials have been designed on the atomic scale with optimal properties. However, solving the quantum mechanical problem for electrons quickly becomes computational expensive when the number of atoms increases up to the hundreds or thousands.

The computational cost of DFT calculations often becomes a limiting factor when trying to predict thermodynamic averages at finite temperatures. This usually requires taking into account configurational degrees of freedom, i.e. composition and ordering. Vibrational degrees of freedom often also plays an important role for thermodynamic properties. Hence thermodynamic sampling often requires calculations for many hundreds, thousands or millions of calculations depending on the problem.

To overcome this problem, models for atomic interactions can be used, where electronic degrees of freedom often are neglected all together. These models are usually trained from DFT and/or experimental data. They are often many orders of magnitude faster when e.g. evaluating the total energy of an atomic configuration

while still retaining good accuracy. There are of course limitations of these models and understanding in which regions the models are accurate and in which they are not is very important. The construction of these models is often non-trivial and can be a very challenging task, specially in regards to training process and understanding the transferability of the models. Examples of atomic-scale models are interatomic potentials, cluster expansions and force constants. Development of software for model construction is part of the present thesis.

The free energy of a system can be used to explain most thermodynamic properties, it is for example necessary when analyze phase stability and when constructing phase diagrams. Free energy of complex systems, even when given an interatomic model, can be tricky to calculate. For example, the free energy of liquids are notoriously difficult to compute. Multi-component systems also poses a sampling problem, which when considering many species is not easily solved. Atomic simulation methods and free energy sampling techniques have also been developed over the years including Monte Carlo and molecular dynamics simulations. Many free energy calculation methods are employed in the present thesis.

2

Cemented Carbides

2.1 General

Cemented carbides, or hardmetals, combine both hardness, the ability to resist plastic deformation, and toughness, the ability to absorb energy and deform plastically without fracturing [1]. These are two competing properties, meaning as one increases the other one tend to decrease. For example, diamond is a very hard material but also brittle (low toughness) and shatters easily. The excellent mechanical properties of cemented carbides make them ideal for usage in diverse applications including high speed machining of steels and in wear resistance tools[2, 3].

The most commonly used cemented carbide is WC-Co which is the material studied in this thesis. The cemented carbide microstructure consists of WC grains forming a continuous skeleton embedded in the Co binder phase. A typical microstructure of WC-Co is shown in Fig. 2.1. The WC grains provide the hardness of the material whereas the Co binder phase adds toughness to the material [4].

2.2 Manufacturing

The WC-Co cemented carbide is manufactured from powders of the carbide and the binder. First, the powders are mixed and milled in order to create an uniform mixture and to reduce the carbide grain size. The milled powders are then pressed to a desired tool shape and then, lastly, sintering takes place [4]. The goal of the sintering is to densify the cemented carbide by eliminating pores, obtain strong inter-grain bonds and achieve a desired microstructure. The sintering is often done in several steps, usually reaching temperatures above 1300 °C where cobalt

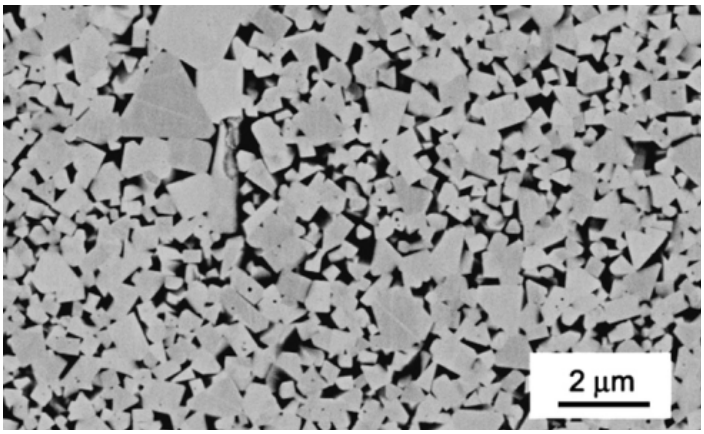

Figure 2.1: Scanning electron microscopy micrograph showing the typical microstructure of WC-Co with at.12% Co, from Ref. [5].

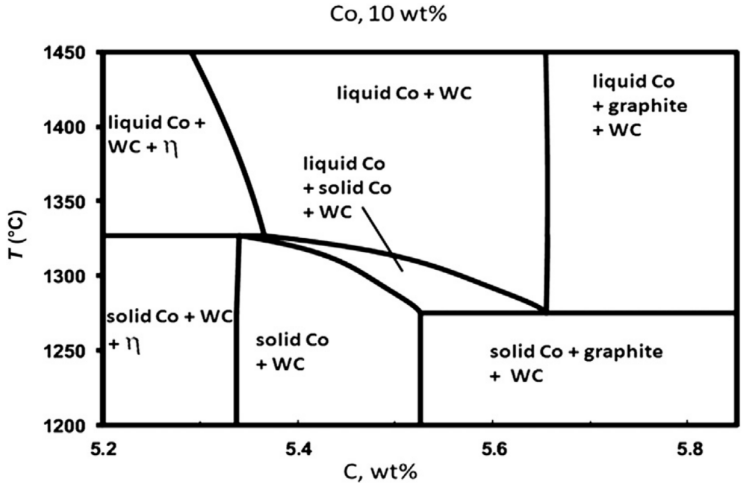

Figure 2.2: Phase diagram of W-C-Co system for a 10 wt% Co as a function of carbon content and temperature, from Ref. [4].

melts. This separates the sintering process into solid-state sintering and liquid-phase sintering.

One important aspect of manufacturing is the carbon content which has a significant impact on the mechanical properties. The phase diagram of W-C-Co for a system with 10 wt% Co as a function of carbon content and temperature is shown in figure Fig. 2.2. When manufacturing, it is desired to be in the two phase, WC-Co, region in order to avoid the formation of either η-phases or graphite. If the carbon content is too low complex carbides denoted η-phases will form. At low temperatures the η_{12}-phase ($M_{12}C$) will form, whereas at temperatures above 1150 °C the η_6-phase (M_6C) will form [6]. The η-phases are brittle and are, therefore, detrimental to the mechanical properties of the cemented carbide. If the carbon content is too high graphite will form which reduces the strength of the cemented carbide.

2.3 Microstructure

The microstructure of cemented carbides, shown in Fig. 2.1, consists of WC grains forming a continuous skeleton in the Co binder phase. The WC grains are shaped as truncated prisms since this shape yields the lowest overall interface energy [7]. Typically, WC grain size ranges from 200 nm to 10 μm [4]. The evolution of the microstructure during manufacturing is driven by the reduction of the total interface free energy in the system, which can be done via reducing the interface area and reorienting grains to find favorable interface orientations. Understanding the interfacial free energies both at zero Kelvin at liquid-phase sintering temperatures can, thus, help to understand and predict the microstructure.

The mechanical properties of the cemented carbide WC-Co is closely connected to its microstructure [5]. Specifically, the size of the WC grains has a significant impact on the mechanical properties, where smaller grains yields a harder material. Due to the inverse proportionality between hardness and toughness a finer microstructure also results in a decrease in toughness [5, 8]. The relation between hardness and toughness has been speculated to change for ultra fine microstructure with grains smaller than 100 nm [8]. Because of this, it is often desirable to keep the grain size as small as possible in order to obtain a hard material.

2.4 Grain growth inhibition

Grain growth is driven by a reduction in overall interface free energies since a few large grains have less interface area than many smaller grains. This can happen via so called Ostwald ripening, where smaller grains are dissolved and, after diffusion, redeposited on larger grains [9]. In WC-Co the grain growth is slow and thought to

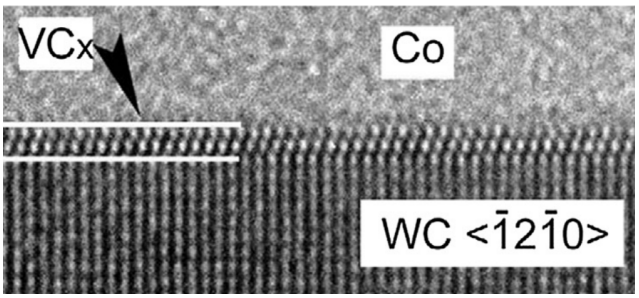

Figure 2.3: High resolution transmission electron microscopy image of a thin cubic VC film from Ref. [15].

be limited via interfacial processes rather than diffusion in the binder phase [10]. Meaning it is likely that either the nucleation of a new atomic layer or the interface mobility is limiting the growth rate. Grain growth in WC-Co have recently been modeled via simulations in Ref. [11]. In this work the rate limiting process was found to be dependent on the grain size, where smaller grains we're limited by nucleation of atomic layers and larger grains limited by the interface mobility.

The grain growth rate can be inhibited via addition of so called grain growth inhibitors [12]. The most common grain growth inhibitors are the transition metals such as V, Ti, Cr, Ta, Mo and Nb [13], where the most potent is V [12]. It is reasonable to believe that the inhibitors in some way interfere with the processes at the interfaces as these are likely the rate limiting processes. These dopants are frequently observed in the phase boundaries between WC and Co where they form thin films. The films exhibit a cubic rocksalt stacking which differs from the ground-state WC hexagonal stacking. In general, the cubic films most often form on the WC basal plane in contact with cobalt, but films can also form on the WC prismatic planes [14]. It is probable that the cubic films are related to the grain growth inhibition effect the dopants have. Thus, it is important to understand under which conditions these films can form in order to e.g. be able to tailor the sintering conditions to achieve a desired microstructure.

2.5 Cubic thin films

2.5.1 Experimental observations

Thin cubic VC films have been observed when doping the WC-Co system with the cubic carbide VC [16, 17, 18]. These films are found to be about 1-2 VC layers thick, a high resolution transmission electron microscopy (HRTEM) image of a film is shown in Fig. 2.3.

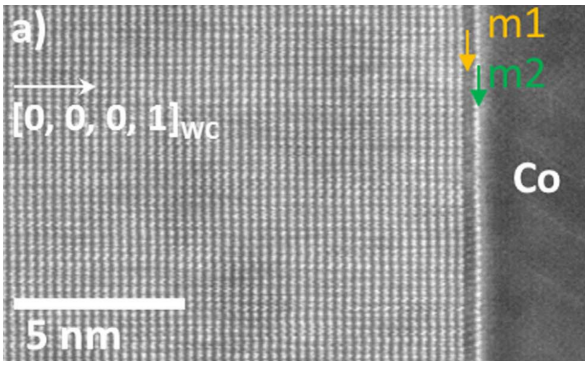

Figure 2.4: Scanning transmission electron microscopy image of a cubic TiC film from Ref. [19].

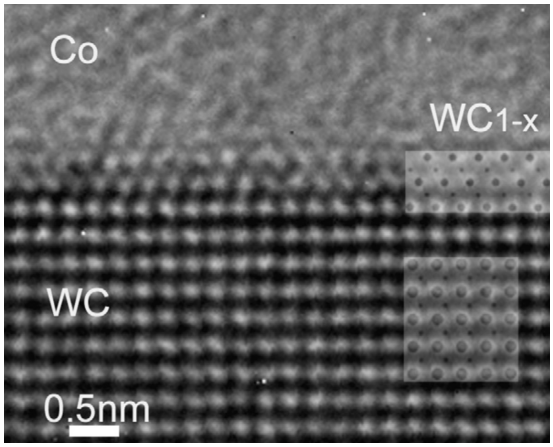

Figure 2.5: High resolution transmission electron microscopy image of a two layer thick cubic film at the phase boundary between the basal WC plane and Co from Ref. [20].

Films have also been observed when doping with the cubic carbide TiC [14, 19], an example is shown in Fig. 2.4. This TiC film from the more recent study, Ref. [19], shows an interesting behaviour where the Ti atoms are located not in the first cubic metal layer (counted from cobalt) but in the second. In this study it is also noted that when measuring the spacing between metal layers in the cubic film there is a significant deviation from ab-initio calculated values. This behaviour is also found in paper I, in which undoped films are studied, where carbon vacancies are shown to drastically reduce the layer spacings in the film. Hence, it is probable that this observed TiC film also contains a significant amount of carbon vacancies.

Even in the undoped WC-Co systems cubic films have been observed [20, 21, 22],

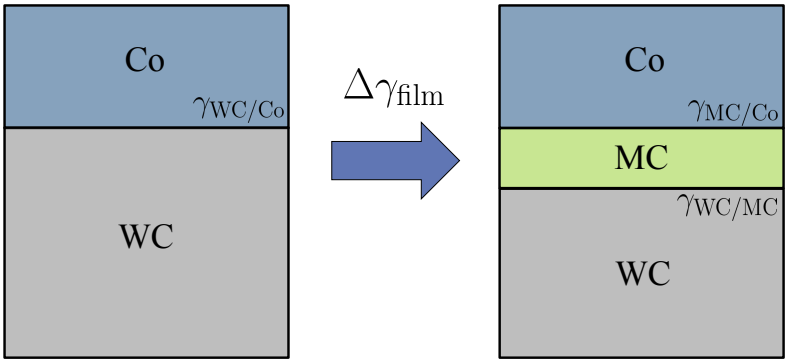

Figure 2.6: Schematic representation of the creation of a thin film. Here MC represents a cubic carbide film with for example M=(W, Ti, V).

a HRTEM image of such a film is shown in Fig. 2.5. These films are 2-4 layers thick and observed on the WC basal plane (0001) with an (111) orientation of the cubic phase. In Ref. [22] films were also observed films on prismatic planes. In Ref. [20] it is stated that cubic films in undoped WC-Co are seldom found in the C-rich materials, whereas very frequently in the W-rich materials. This can be understood from the fact that the WC cubic phase contains a high concentration carbon vacancies whereas the hexagonal WC phase is very stoichiometric [23]. In W-rich materials the carbon chemical potential is lower compared to C-rich materials, this means that the cubic WC films (containing carbon vacancies) are more stable in the W-rich materials.

2.5.2 Simplified modeling

The stability of cubic thin films can to a large extent be understood from a simplified model as demonstrated in Ref. [24]. The formation of a film can be thought of inserting a thin region of cubic MC at the phase boundary, as illustrated in Fig. 2.6. The system goes from having one interface WC/Co to having two, WC/MC and MC/Co. In order for the thin film to be stable it is thus a necessity that the sum of two latter interface energies are lower than the starting interface energy, i.e.

$$\gamma_{\mathrm{WC/MC}} + \gamma_{\mathrm{MC/Co}} < \gamma_{\mathrm{WC/Co}}, \tag{2.1}$$

where $\gamma_{\mathrm{X/Y}}$ denotes the interface energy between the two phases X and Y. Even if this condition is met, creating the film also comes with an associated cost of creating the MC phase of $\Delta g_{\mathrm{MC}} + e_{\mathrm{MC}}$ per MC-layer. Here, Δg_{MC} denotes the cost of creating the cubic MC phase compared to the equilibrium phases and e_{MC}

M	$\gamma_{\mathrm{WC/Co}}$	$\gamma_{\mathrm{WC/MC}}$	$\gamma_{\mathrm{MC/Co}}$	e_{MC}	Δg_{MC}	$\Delta\gamma_{\mathrm{film}}(N=2)$
V	1.12	0.03	-0.01	0.01	0.00	-1.08
Ti	1.12	-0.33	0.82	0.40	0.00	0.17
W	1.12	0.42	-1.29	0.40	2.03	2.87

Table 2.1: The relevant interface energies and associated cost for creating the cubic phase given for V, Ti and W. All values are given in $\mathrm{J/m^2}$.

denotes the strain energy associated with the misfit between the hexagonal WC phase and the film. In total, a film of N MC-layers is stable if the formation energy of the film, $\Delta\gamma_{\mathrm{film}}$, defined as

$$\Delta\gamma_{\mathrm{film}}(N) = \gamma_{\mathrm{WC/Co}} - \left[\gamma_{\mathrm{WC/MC}} + \gamma_{\mathrm{MC/Co}} + N(\Delta g_{\mathrm{MC}} + e_{\mathrm{MC}})\right]$$

is negative. This estimate of the formation energy of the film becomes less reliable when N is very small. Values for the relevant interface energies are shown in Table 2.1 for a for V and Ti doped films [25] as well as the undoped film, where the film is placed on the basal plane with the following orientation

$$\mathrm{WC}_{\delta}(0001) \parallel \mathrm{WC}_{\gamma}(111) \parallel \mathrm{Co}(111)$$

where WC_{δ} and WC_{γ} corresponds to the hexagonal and cubic phases, respectively. It is clear from Table 2.1 that all three films fulfill Eq. (2.1). For the V films $\Delta\gamma_{\mathrm{film}}$ (assuming two MC layers) is negative, meaning VC films are stable. In the case of Ti a small but positive value is obtained, indicating the possibility of film formation.

Ti segregating to the second cubic layer, as was reported in Ref. [19] (see Fig. 2.4), can also be qualitatively understood from this simplified model. TiC have a large interface energy towards Co, $0.82\,\mathrm{J/m^2}$, whereas the cubic WC phase have a very favorable interface towards Co, $-1.29\,\mathrm{J/m^2}$. Hence, changing the first Ti layer to W would yield a reduction in interface energy, $\gamma_{\mathrm{MC/Co}}$, of $-2.11\,\mathrm{J/m^2}$ which would compensate for the bulk cost of changing a cubic Ti layer to W of $2.03\,\mathrm{J/m^2}$.

For the undoped cubic films the formation energy is very large, $2.87\,\mathrm{J/m^2}$, yet these films are frequently observed in experimental studies. In order to understand this we must thus go beyond this simplified modeling.

2.5.3 Extensive modeling

V-doped films have been extensively studied in Ref. [26]. In this work cluster-expansions were employed to model the mixing of W and V atoms on the cubic lattice sites in the film. This allowed for the interfacial phase diagram of the

system to be constructed as a function of V chemical potential and temperature. It also allows for more precise prediction of the ordering of V and W atoms in the cubic film. Further calculations predicted that even at liquid-phase sintering temperatures and low doping concentration, for which the cubic (W,V)C bulk phase is not thermodynamically stable, the cubic VC films was stable. In paper I we employ similar methodology in order to understand cubic films in undoped WC-Co. We also extend this method further by including vibrational contributions.

3

Alloy cluster expansions

One of the most common lattice based interatomic model is the so-called alloy cluster expansion. They are based on a static lattice where the degrees of freedom are the occupation of the lattice. The main idea is to decompose an atomic structure into its corresponding clusters. Associating each clusters with e.g. an energy then allows for predicting the total energy of the structure. Predictions of properties of a structure, e.g. total energy, using cluster expansions are very fast. This makes studying thermodynamics for configurational degrees of freedom feasible.

3.1 Clusters

An atomic structure is composed of a set of lattice points, a cell and occupations $\boldsymbol{\sigma}$ corresponding to which atomic species occupies which lattice point. A cluster is defined as a collection of unique lattice points. The order of the cluster is given by the number of lattice points, for example, two lattice points corresponds to a pair. Clusters can be grouped into orbits or neighbor shells, i.e. first nearest neighbor pair, second nearest neighbor pair and so on. This can easily be imagined for simple lattices, such as the simple cubic one illustrated in Fig. 3.1, whereas for more complex systems and higher order clusters it becomes more complicated to construct orbits of clusters. The definition of an orbit used here (and in ICET and HIPHIVE) is the collection of all symmetrically equivalent clusters. Two clusters are thought to be equivalent if they can transformed into each other by lattice symmetries, where a lattice symmetry consists of a rotation $\boldsymbol{R}$ and a translation $\boldsymbol{t}$. Applying a lattice symmetry to lattice point coordinate $\boldsymbol{r}$ is done via

$$\tilde{\boldsymbol{r}} = \boldsymbol{R} \cdot \boldsymbol{r} + \boldsymbol{t}$$

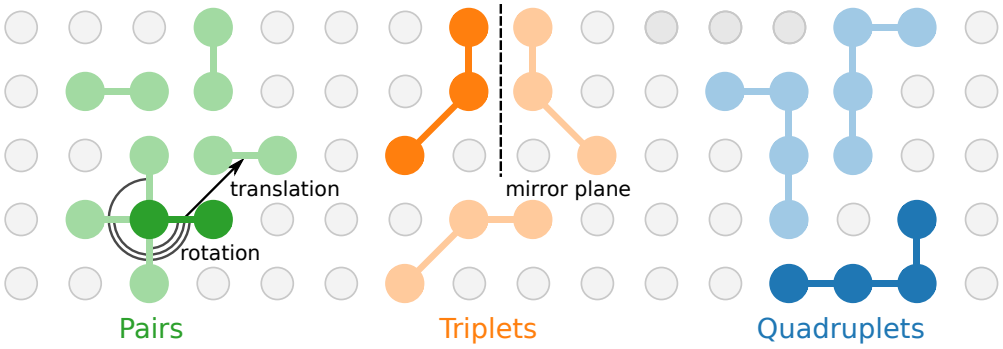

Figure 3.1: Illustration of a simple cubic lattice with pairs (green), triplets (orange) and quadruplets (blue) highlighted. All clusters of the same order can be transformed into each other under some lattice symmetries, a few of which are illustrated.

where $\tilde{\boldsymbol{r}}$ is the position of a new lattice point. Transforming all lattice points with a lattice symmetry leaves the lattice unchanged (save a permutation of ordering of lattice points). So if lattice points (i, j) are mapped to lattice points (k, l) using lattice symmetry operation number s, e.g.

$$(i, j) \overset{\boldsymbol{R}_s, \boldsymbol{t}_s}{\longrightarrow} (k, l)$$

then the cluster (i, j) is said to be symmetry equivalent to (k, l) and they therefore belong to the same orbit. This is illustrated in Fig. 3.1, where all clusters of the same order is symmetrically equivalent.

3.2 Cluster Expansion

Cluster expansions can describe any property Q which is a function dependent on the occupation $\boldsymbol{\sigma}$ of the lattice as

$$Q(\boldsymbol{\sigma}) = Q_0 + \sum_{\boldsymbol{\alpha}} \langle \Pi_{\boldsymbol{\alpha}'}(\boldsymbol{\sigma}) \rangle_{\boldsymbol{\alpha}} \, m_{\boldsymbol{\alpha}} J_{\boldsymbol{\alpha}} \tag{3.1}$$

where $\Pi_{\boldsymbol{\alpha}}$ are basis functions, $m_{\boldsymbol{\alpha}}$ the multiplicity the orbit and $J_{\boldsymbol{\alpha}}$ are the effective cluster interactions (ECIs). The full formalism can be found in Paper III and in literature Ref. [27].

In order to find the unknown parameters of the model $J_{\boldsymbol{\alpha}}$, training structures are required. For training structure i with occupation $\boldsymbol{\sigma}_i$ and quantity Q_i the cluster

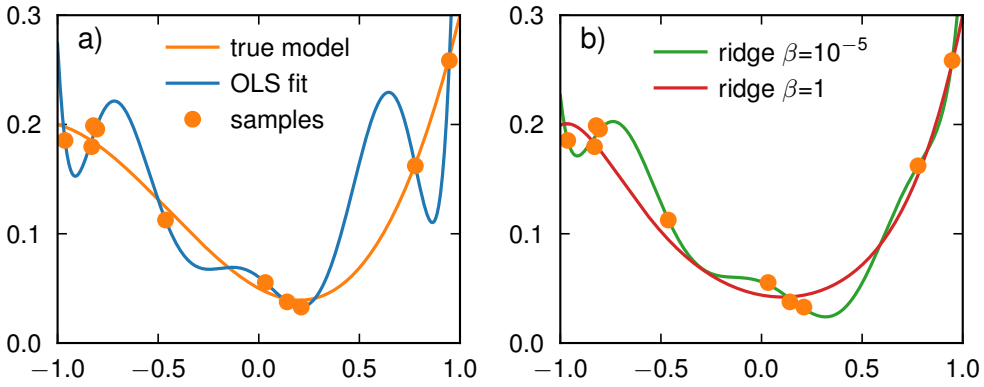

Figure 3.2: Illustration of reconstruction of a polynomial model from data (samples) with noise. a) The true model and model obtained from ordinary least squares (OLS) using the shown samples as training data. The OLS model shows clear signs of overfitting. b) Two models constructed using ridge regression with different values of β (see Eq. (3.2)) showing how overfitting can be reduced.

vector can be constructed via

$$\boldsymbol{\Pi}_i = (1, \langle \Pi_{\boldsymbol{\alpha}'}(\boldsymbol{\sigma}_i) \rangle_{\boldsymbol{\alpha}} m_{\boldsymbol{\alpha}})$$

where $\boldsymbol{\Pi}_i$ refers to the cluster vector of structure i and the starting 1 is included in order to pick up the first term in Eq. (3.1). This yields a linear system of equations

$$\boldsymbol{Q} = \boldsymbol{\Pi} \boldsymbol{J}$$

which can be solved in order to obtain the ECIs.

3.3 Linear regression

There are many different linear regression methods available. In the overdetermined limit the problem can be solved by ordinary least squares (OLS). Least squares provides the solution which minimizes the root-mean-square error (RMSE) for the training structures. RMSE is defined as

$$\text{RMSE} = \sqrt{\frac{1}{N} \sum_i \left(Q_i^{\text{target}} - Q_i^{\text{predicted}} \right)^2}$$

where N is the number of structures. OLS tend to lead to overfitting, meaning the model has learned too many details in the training structure, causing low predictive

power for unseen structures. Overfitting can be reduced by regularization, i.e. addition of a penalty term in the objective function

$$\|\boldsymbol{\Pi}\boldsymbol{J} - \boldsymbol{Q}\|_2^2 + \alpha\|\boldsymbol{J}\|_1 + \beta\|\boldsymbol{J}\|_2^2 \tag{3.2}$$

where the first term is the objective function for OLS and the two last terms are ℓ_1 and ℓ_2 regularization terms where α and β control their regularization strengths respectively. Setting $\beta = 0$ one obtains the objection function of least absolute shrinkage and selection operator (LASSO) which tends to favor sparse solution vector $\boldsymbol{J}$. For $\alpha = 0$ one recovers the objective function for ridge regression which rather penalizes large elements in $\boldsymbol{J}$ heavily and thus tries to keeps all parameters small.

An example of the effect from regularization is shown in Fig. 3.2. Here, an eighth order polynomial is fitted to training data generated from a polynomial with the addition of small noise. In Fig. 3.2(a) the model trained with OLS describes all training samples very well whereas in between training samples the model performs poorly. This is a clear indication of overfitting. In Fig. 3.2(b) ridge regression is used with two different values of β. Using a very small value a similar model to OLS is obtained. For a larger value of β a less complex model is obtained which generalizes better to regions where no training data exists.

Compressive sampling algorithms, commonly used in signal processing, have been proposed to be very suitable for constructing physical models [28]. In these algorithms ℓ_1 regularization is used, similar to LASSO.

A feature selection algorithm that we have found to work well for cluster expansions is the recursive feature elimination (RFE) method. It requires a linear regression solver and then performs a series of fits. First, all parameters are included in the training procedure, then iteratively a small percentage of the parameters is removed until the desired number of parameters n_f is obtained. This often reduces overfitting and yields very sparse models with high transferability. The optimal value of the hyper-parameter n_f is not known beforehand, similarly to hyper-parameters α and β in Eq. (3.2). These can be determined by e.g. Bayesian optimization [29] or by cross-validation (CV) analysis.

3.3.1 Cross Validation

Cross validation is a way of statistically testing the accuracy of a model. The entire dataset is split into two parts, one used for training (training set) and one used for validating the model (validation set) via e.g. RMSE. This is often repeated multiple times with different splits of the dataset in order to reduce the statistical noise. One of the more common ways of splitting the data is the k-fold method where the dataset is split into k equally large parts. The training is done using $k-1$ parts and the last part is used for validation, which can be repeated k times.

3.3.2 Ensemble of models

In paper III we construct ensembles of models from different splits of the training structures generated with replacement. This means that with N total number of structures a training set is generated by drawing N structures without replacing them, i.e. allowing for duplicates in the training set. Repeating this multiple times to get a statistical estimate of some property is known as bootstrapping [30]. It allows for estimating, to some extent, the variance in thermodynamic proprieties due to variance in training structure selection. In paper III, this is demonstrated for phase diagram construction and chemical ordering analysis.

3.4 Monte Carlo simulations

Once a cluster expansion model is constructed for the total energy of the system it can be used to sample various thermodynamic properties. This is commonly done via Monte Carlo (MC) simulations using the Metropolis algorithm [31].

3.4.1 Canonical Ensemble

In the canonical ensemble the number of atoms, volume and temperature (NVT) are kept fixed. For each atom type α in a multicomponent systems the number of atoms, N_α, is fixed. The MC is carried by first occupying a supercell with the desired number of atoms of each species. Then, trial moves consisting of swapping two atoms (of different species) are carried out which are accepted with a probability

$$P = \min\left(1, \mathrm{e}^{-\beta\Delta E}\right)$$

where $\beta = \frac{1}{k_B T}$, k_B is the Boltzmann constant and ΔE is the change in energy due to the swap. This will generate configurations (microstates) according to the probability $\mathrm{e}^{-\beta E_i}/Z_{N_\alpha VT}$ where the partition function $Z_{N_\alpha VT}$ is defined as

$$Z_{N_\alpha VT} = \sum_i \mathrm{e}^{-\beta E_i}$$

where E_i is the energy of microstate i and the sum extends over all possible microstates with macroscopic properties $N_\alpha VT$ [31]. This allows for thermodynamic properties to be sampled as

$$\langle A \rangle = \sum_i A_i \frac{\mathrm{e}^{-\beta E_i}}{Z_{N_\alpha VT}} \approx \frac{1}{N_{\mathrm{MC}}} \sum_{i \in \mathrm{MC}} A_i$$

where $\sum_{i\in\mathrm{MC}}$ represents a sum over all configurations generated in the MC simulation.

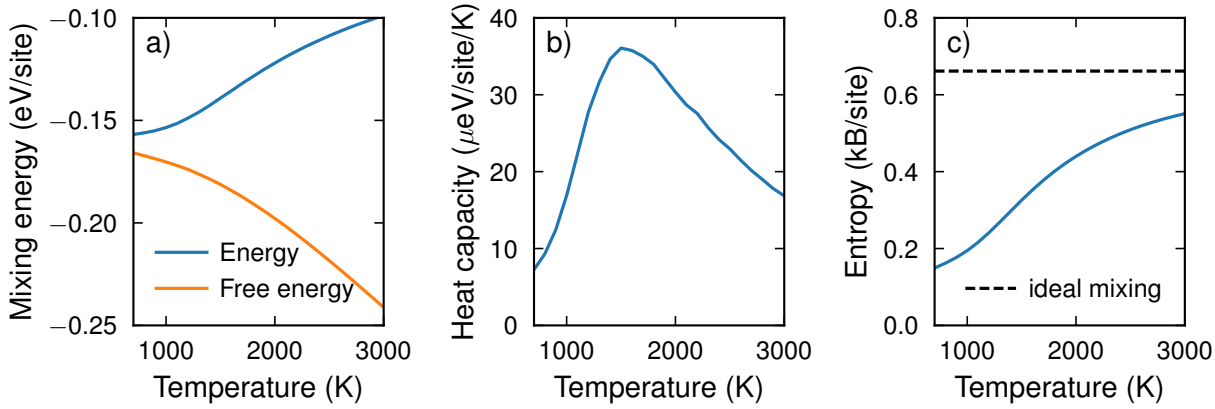

Figure 3.3: Results from MC simulations in the canonical ensemble for the interface denoted k_4 from Paper I with 60% carbon vacancies . a) The mixing energy and free energy as a function of temperature. b) The heat capacity as a function of temperature. c) The obtained entropy as a function of temperature compared to the ideal mixing limit.

3.4.1.1 Entropy integration

The canonical free energy of a system can be calculated using MC simulations in the canonical ensemble. This is demonstrated in the Supplementary information for paper I. The entropy, $S(T)$, is obtained by integrating the heat capacity $C_v(T)$ over temperature. By recording the energy $E(T)$ from a MC simulation the heat capacity can be calculated as

$$C_v(T) = \frac{\langle E(T)^2 \rangle - \langle E(T) \rangle^2}{k_B T^2}.$$

The entropy $S(T)$ can then calculated via

$$S(T) = S(\infty) + \int_{\infty}^{T} \frac{1}{T} C_v(T) \mathrm{d}T$$

where $S(\infty)$ is known from ideal mixing. The free energy can finally be obtained by

$$F(T) = E(T) - TS(T).$$

In Fig. 3.3 the thermodynamic properties (E, F, C_v and S) obtained from MC simulations and integration are shown for the interface system k_4 from paper I with

a vacancy concentration of 60%. As expected the entropy approaches zero for low temperatures and the value corresponding to ideal mixing for high temperatures. This free energy integration method is very similar to the temperature integration carried out using molecular dynamics in paper II.

3.4.2 Grand Canonical Ensemble

In the grand canonical ensemble the chemical potentials, volume and temperature ($\mu_\alpha VT$) are kept fixed. The system is thought to be in equilibrium with reference states with chemical potentials μ_α. The partition function is defined as

$$Z_{\mu_\alpha VT} = \sum_i \mathrm{e}^{-\beta(E_i - \sum_\alpha N_{i\alpha}\mu_\alpha)}$$

where $N_{i\alpha}$ denotes the number of atoms of type α for microstate i [31, 32]. Here the summation extends over all possible microstate not limited to specific values of N_α as in the case of the canonical ensemble. In grand canonical ensemble MC trial move consists of either inserting or removing a single atom, accepted with a probability of

$$P = \min\left(1, \mathrm{e}^{-\beta(\Delta E - \sum_\alpha \Delta N_\alpha \mu_\alpha)}\right)$$

where ΔN_α is the change in number of atoms for species α [31]. In paper I we demonstrate and explain how this ensemble can be used to sample the canonical free energy.

4

Force constant models

Force constant models, while also based on a lattice, describes the vibrational motion for a fixed occupation of a lattice.

4.1 Formalism

The potential energy, E, can be expressed as a Taylor expansion

$$E = E_0 + \Phi_i^\alpha u_i^\alpha + \frac{1}{2}\Phi_{ij}^{\alpha\beta} u_i^\alpha u_j^\beta + \frac{1}{3!}\Phi_{ijk}^{\alpha\beta\gamma} u_i^\alpha u_j^\beta u_k^\gamma + \dots, \tag{4.1}$$

where Φ are the force constants, Latin indices enumerates the atoms, Greek indices enumerate the Cartesian coordinates, and the Einstein summation convention is implied. Here, u describes the displacements from some static positions r_0, usually chosen as an ideal lattice for which the first order term in the expansion is zero. E_0 corresponds to the static energy for the static positions r_0. The unknowns in this model are the force constants, where e.g. second order force constants are defined as

$$\Phi_{ij}^{\alpha\beta} = \frac{\partial E}{\partial u_i^\alpha u_j^\beta}, \tag{4.2}$$

and analogously for other orders. The number of force constants in the expansion grows rapidly as the number of atoms and order is increased, however, similar to the case of cluster expansions, symmetries can reduce the number of independent degrees of freedom significantly. One difference compared to cluster expansion is that terms like Φ_{001} shows up in Eq. (4.1) which corresponds to a third order pair interaction. It is often useful to distinguish force constants by both order and n-body (number of atoms in the interaction), specially since higher order pair terms

are often important whereas the strength of n-body interactions often decrease rapidly with n.

Force constants can conveniently be obtained using the direct approach [33], where the derivatives are numerically computed by calculating forces of configurations with single atoms being displaced. This method works very well and is implemented in many different softwares, PHONOPY [33] for second-order and PHONO3PY[34], SHENGBTE[35], ALMABTE [36], and AAFLOW [37] for third-order force constants. However, for systems with low symmetry, e.g. defective or interfacial systems, this method quickly becomes computational expensive due to the large number of supercell calculations required.

4.2 Regression approach

Another approach is to extract the force constants via regression. This has been shown to produce accurate force constants [38, 39, 40, 41, 42, 43, 44]. In paper IV we introduced the python package HIPHIVE for this purpose. Fitting the force constants has the advantage of not requiring as many calculations. This is possible since the information obtained from calculations where only one atom is displaced is quite small whereas when fitting force constants all atoms may be displaced giving rise to much more information.

The parametrization of the force constants, including symmetries and sum rules, are explained in detail in paper IV. Using this parametrization and a set of supercells with displacements and forces, a linear problem is obtained to solve for the independent degrees of freedom

$$\boldsymbol{F} = \boldsymbol{A}\boldsymbol{x},$$

where $\boldsymbol{F}$ is the forces for all supercells, $\boldsymbol{A}$ the fitting matrix and $\boldsymbol{x}$ the unknown parameters. To solve this similar techniques as described in Sect. 3.3 can be used. Although the dimensionality of the linear problem for force constants is often quite large, up to tens of thousands rows and columns in $\boldsymbol{A}$ making some of the computational more expensive linear regression techniques unfeasible to use. In paper V a brief comparison of the performance of a few different linear regression methods is carried out. In order to obtain accurate force constants the truncation of the expansion along with the linear regression method and its hyper parameters need to be chosen careful. The method that consistently performed well for our examples was combining RFE with OLS.

4.3 Harmonic models

The vibrational properties of a solid is fundamental in understanding many of its properties. A force constant model can be sampled in various ways, the simplest being a harmonic approximation. In the harmonic approximation only the second order force constants (assuming first order are zero) are considered. The dynamical properties of a crystal in the harmonic approximation is obtained by constructing the dynamical matrix $\boldsymbol{D}(\boldsymbol{q})$ for a reciprocal wave vector $\boldsymbol{q}$. Following the notation in [33] it can be calculated via

$$D^{\alpha\beta}_{\kappa,\kappa'} = \sum_{l'} \frac{\Phi^{\alpha\beta}_{0\kappa,l'\kappa'}}{\sqrt{m_\kappa m_{\kappa'}}} \mathrm{e}^{-i\boldsymbol{q}\cdot(\boldsymbol{r}_{0\kappa}-\boldsymbol{r}_{l'\kappa'})},$$

where $l\kappa$ corresponds to basis atom κ in primitive cell l, $\boldsymbol{r}$ the position and m the mass. The harmonic frequencies can then be obtained by solving the eigenvalue problem

$$\boldsymbol{D}(\boldsymbol{q})\boldsymbol{e}_{\boldsymbol{q}j} = \omega^2_{\boldsymbol{q}j}\boldsymbol{e}_{\boldsymbol{q}j}$$

where $\omega_{\boldsymbol{q}j}$ is the harmonic frequency at $\boldsymbol{q}$ with mode index j and $\boldsymbol{e}_{\boldsymbol{q}j}$ the corresponding eigenvector. Given the harmonic frequencies many other vibrational properties can be extracted, e.g. phonon dispersion, density of states, potential energy, heat capacity, entropy and free energy [45, 33]. The harmonic free energy, $F(T)$, is given by

$$F(T) = \sum_{\boldsymbol{q}j} k_B T \ln\left(1 - e^{-\frac{\hbar\omega_{\boldsymbol{q}j}}{k_B T}}\right) + \frac{1}{2}\hbar\omega_{\boldsymbol{q}j}$$

where the last term corresponds to the zero point motion. The static potential energy of the lattice, E_0, can be included in this equation to obtain the full free energy of the system.

4.3.1 Quasi harmonic approximation

Phonon modes tend to soften when the volume is increased due to weaker bonds between atoms. Lower frequencies give rise to a larger vibrational entropy meaning volume tend to increase with temperature. Thermal expansion is an anharmonic effect which is neglected in the harmonic approximation. This effect can be treated using the quasi-harmonic approximation (QHA) in which harmonic models are constructed for multiple different volumes. These models are used to extract the harmonic free energy $F(V,T)$, which allows for finding the equilibrium volume

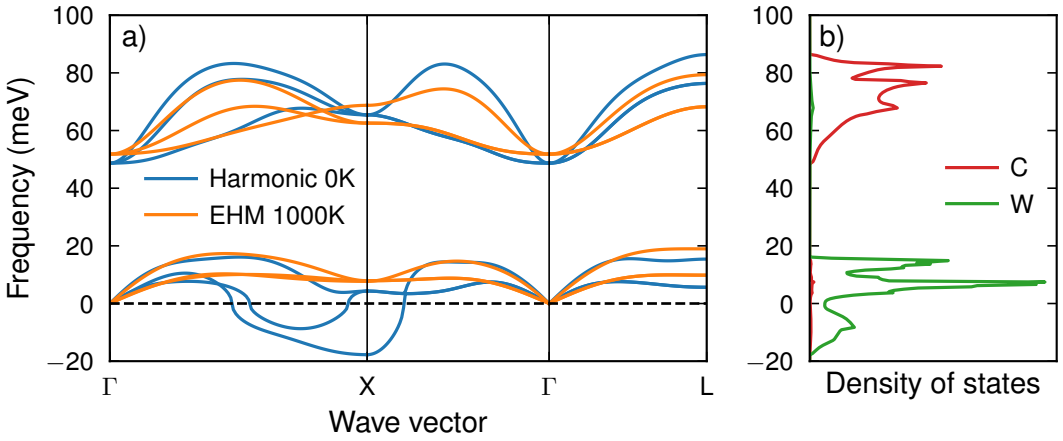

Figure 4.1: a) Phonon dispersion for cubic WC for a regular harmonic model (denoted 0 K) and an effective harmonic model computed from an ab-initio molecular dynamics (MD) simulation at 1000 K. b) Partial density of states for the regular harmonic approximation.

$V_{eq}(T)$ via

$$V_{eq}(T) = \underset{V}{\operatorname{argmin}}\, F(V, T).$$

In paper II the quasi harmonic approxmiation is employed to the WC hexagonal bulk phase which has two lattice parameters a and c. In this case, to find the equilibrium lattice parameters, the minimization is carried simultaneously with respect to both lattice parameters, i.e.

$$(a_{eq}(T), c_{eq}(T)) = \underset{a,c}{\operatorname{argmin}}\, F(a, c, T).$$

The harmonic free energy can be expressed as a function of other geometrical parameters of your system as well. In Ref. [46] the surface layer spacing d is computed as a function of temperature for a Ag (111) surface by writing the harmonic free energy as $F = F(d, T)$. This allows, analogously to QHA, for extraction of the layer spacing d corresponding to the lowest free energy as a function of temperature.

4.3.2 Effective harmonic models

One of the simpler, yet very powerful methods to account for anharmonicity is to compute effective harmonic models from MD simulations [47, 48, 49]. The basic

idea is that the harmonic model constructed from displacements and forces from an MD simulation will effectively incorporate anharmonic effects. Once the effective harmonic model is constructed it can be used as a regular harmonic model to predict temperature dependent properties, however the accuracy of the model is best close to the temperature from which it was constructed.

A good example where effective harmonic models (EHMs) are useful is the WC cubic phase which is thermodynamically stable at higher temperature [23], but dynamically unstable at low temperature. The EHM technique is demonstrated in figure Fig. 4.1 together with the regular harmonic approximation, denoted 0 K. The regular harmonic model have imaginary frequencies, shown as negative, indicating structural instabilities, whereas in the EHM these modes are stable. From the partial density of states it is also clear that the high frequencies corresponds to carbon modes and low frequencies W modes as expected due to the mass discrepancy.

4.3.2.1 Zwanzig correction

For obtaining accurate free energies using effective harmonic models free energy perturbation can be applied [50]. It describes the free energy difference between two Hamiltonians A and B as

$$F_A - F_B = \frac{1}{\beta} \ln \left\langle \mathrm{e}^{-\beta(E_B - E_A)} \right\rangle_A , \tag{4.3}$$

where E_A and E_B is the energy for Hamiltonian A and B respectively, and $\langle ... \rangle_A$ denotes an ensemble average carried out in Hamiltonian A. In the case of EHMs the EHMs correspond to Hamiltonian B and the reference potential energy surface (often DFT) to A. Thus a correction to the effective harmonic free energy using the free energy perturbation method is obtained providing a better estimate of the free energy of the reference system A. This correction can conveniently be applied as the EHM is constructed from MD and thus the ensemble average in Eq. (4.3) can easily be evaluated. This free energy perturbation correction is similar to the correction carried out in Ref. [49] where E_0 from Eq. (4.1) is determined in order to minimize $\langle E_A - E_B \rangle_A$.

4.4 Higher order models

Third order force constants can be used to calculate phonon lifetimes in a perturbation theory [45]. Phonon lifetimes can, for example, be used to compute the lattice thermal conductivity via Boltzmann transport theory [34].

Fourth order force constants can be used to, for example, renormalize the harmonic frequencies via self consistent phonons[45]. This has been done successfully

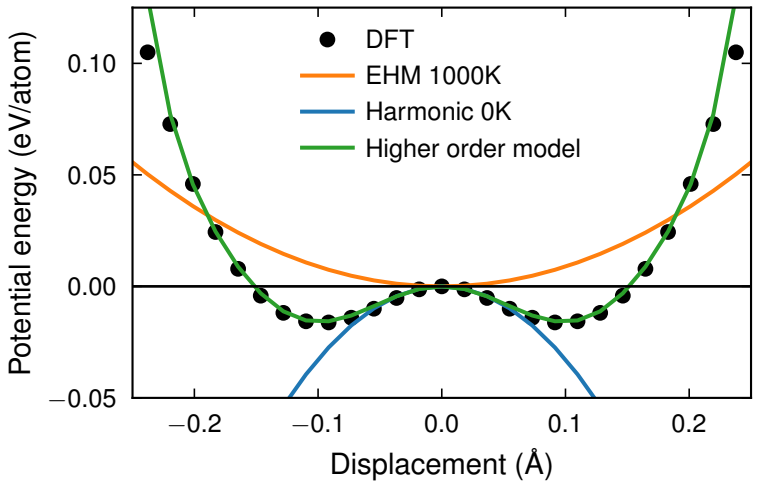

Figure 4.2: Potential energy landscape for the cubic WC phase along the imaginary phonon mode at X, constructed using DFT, an effective harmonic model at 1000 K, a regular harmonic model and a higher order models. The x-axis corresponds to the average displacement of all atoms along the phonon mode.

[51, 42], and has the benefit compared to effective harmonic models that only one force constant model needs to be constructed which can then be used for a wide temperature range.

Higher order models can also be used more directly to map out the potential energy surface. This is demonstrated in Fig. 4.2, where the energy landscape of the imaginary mode of the cubic WC phase at the X point (see Fig. 4.1) is shown. The energy landscape is constructed directly using DFT, the harmonic model, an EHM from 1000 K and a sixth order model. The higher order model is trained from them same data as the EHM, as well as data along the phonon mode path. This is not meant to be optimal higher order model for the cubic WC phase but rather illustrate that these type of anharmonic energy landscape are easily reproduced with higher order models. Fig. 4.2 also highlights the fact that in the harmonic approximation the mode is unstable but stabilized with an effective harmonic model at 1000 K.

Higher order models can also be used to run MD simulations from which thermodynamic properties can be extracted [39]. This is illustrated in the clathrate application in paper V, where the temperature dependency of phonon frequencies is directly sampled from MD simulations. A problem with this approach is that, in general, the force constant potentials are not stable when truncating the expansion (by interaction length and order). This problem was also noted in recent work,

Ref. [40], where inclusion of short ranged strongly anharmonic pair potentials were successfully used to stabilize the potential.

At some point, though, the anharmonic effects and tendencies for diffusion becomes too large to treat with force constants and one must turn to other ways to model the potential energy surface.

5

Interatomic potentials

Interatomic potentials are in general more flexible than cluster expansions and force constant models. The potential energy E is often written as

$$E = E(\boldsymbol{r}_1, \ldots, \boldsymbol{r}_i, \ldots, \boldsymbol{r}_N)$$

where $\boldsymbol{r_i}$ is the position of atom i and N the total number of atoms. Implied here is also the knowledge about the atom types. Interatomic potentials are not limited to solids or a fixed lattice but applicable also to both liquid and gas phases.

5.1 Pair potentials

The simplest form of a potential is a pair potential, in which the potential energy is only dependent on the interatomic distances in the system. One of the more well known pair potentials is the Lennard-Jones potential [52], which can be written as

$$E = \sum_{i<j} 4\varepsilon \left[\left(\frac{\sigma}{r_{ij}} \right)^{12} - \left(\frac{\sigma}{r_{ij}} \right)^{6} \right]$$

where r_{ij} is the distance between atom i and j. ε and σ are the free parameters of the potential which controls the energy and length scale respectively. Pair potentials such as Lennard-Jones works well for systems with noble gas atoms, but fails when many-body effects are important.

5.2 Embedded atom model

The embedded atom method (EAM) consists of a pair potential and an additional term that represents the energy cost of embedding an atom in an electron density

from the surrounding atoms. This works specifically well to model the many-body effects in metallic systems. The functional form of an EAM is usually written as

$$E = \sum_{i<j} \phi(r_{ij}) + \sum_i F\left(\sum_{j\neq i} \rho(r_{ij})\right)$$

where $\phi(r_{ij})$ is the pair potential, F the embedding function and ρ_i the density function. Here, the functional forms of ϕ, F and ρ are the free degrees of freedom of the potential. There exists multiple variants of this potential form named EAM [53], effective medium theory (EMT) [54] and Finnis-Sinclair [55]. While the usage of EAM have been very successful, the potential form does not describe directional bonding very well which is crucial for covalent systems such as WC.

5.3 Analytical bond order potentials

An effective way of dealing with strong directional bonding is to add three body terms to the interatomic potential. An example of this is the analytical bond order potential (ABOP)[56, 57, 58], written as

$$E = \sum_{i<j} f^c(r_{ij}) \left(V^R(r_{ij}) - b_{ij} V^A(r_{ij})\right)$$

where V^R and V^A are repulsive and attractive Morse-like pair potentials respectively and f^c a cutoff function which decays towards zero as the interatomic distance increases. Here b_{ij} is a functional of a three-body term.

In paper II we employ a ABOP for calculating interface free energies in the WC-Co system at finite temperatures. This potential was constructed using parameters for C-C interactions from Ref. [58], W-C interactions from Ref. [59], C-Co and W-Co from Ref. [60].

5.4 Molecular dynamics

Thermodynamic sampling using interatomic potentials can often be carried out effectively via MD simulations [61]. In MD the atomic positions and velocities is evolved in time using classical mechanics and an interatomic potential according

$$m_i \frac{\partial^2 \boldsymbol{r}_i(t)}{\partial t^2} = \boldsymbol{f}_i(t) \tag{5.1}$$

$$\frac{\partial \boldsymbol{r}_i(t)}{\partial t} = \boldsymbol{v}_i(t) \tag{5.2}$$

where m_i, $r_i(t)$, $v_i(t)$ and $f_i(t)$ is the mass, position, velocity and force for atom i at time t. The force acting on an atom $\boldsymbol{f}_i(t)$ is computed via the interatomic potential as

$$\boldsymbol{f}_i(t) = -\frac{\partial E(\boldsymbol{r}_1(t), \ldots, \boldsymbol{r}_N(t))}{\partial \boldsymbol{r}_i}.$$

The integration of the equation of motions, Eq. (5.2), is carried out numerically for discrete times, often using the Verlet algorithm [62]. This will result in sampling in the microcanonical ensemble (NVE) since the system is isolated and, thus, the total energy in the system is constant. The temperature, using the equipartition theorem, is given by

$$T = \frac{2}{3k_B}\left\langle \frac{1}{2} m|\boldsymbol{v}|^2 \right\rangle,$$

where $\langle ... \rangle$ denotes the ensemble of the kinetic energy per atom [61]. If the system is ergodic ensemble averages can be changed to time averages, which are easily computed in MD simulations. For example, for a quantity A the thermodynamic average can be computed by

$$\langle A \rangle = \frac{1}{N_{\text{steps}}} \sum_t A(t)$$

where the sum $\sum_t$ is over the MD trajectory and N_{steps} is the total number of timesteps.

5.4.1 Thermodynamic integration

One very effective way of calculating free energies using MD is thermodynamic integration between two Hamiltonians, H_A and H_B. Here, A represent the system for which the free energy is desired and B a system for which the free energy is known. Constructing a Hamiltonian H as

$$H(\lambda) = (1-\lambda)H_A + \lambda H_B \tag{5.3}$$

allows for the free energy difference between A and B to be computed via

$$F_B - F_A = \int_0^1 \left\langle \frac{\mathrm{d}H(\lambda)}{\mathrm{d}\lambda} \right\rangle_H \mathrm{d}\lambda \tag{5.4}$$

where the integration is carried out over the Kirkwood coupling parameter λ [63]. Here the ensemble average $\langle ... \rangle_H$ should be carried out using the full Hamiltonian

H. The linear mixing between H_A and H_B in Eq. (5.3) is not required but makes the integral in Eq. (5.4) easy to evaluate.

The Hamiltonian H_B needs to be chosen such that its the free energy is known. One common choice of B is an Einstein solid, which is referred to as the Frenkel-Ladd method [64]. In an Einstein solid the dynamics are described by independent harmonic oscillator with a frequency ω_E. The free energy of an Einstein solid, F_E, is known as

$$F_E = 3Nk_BT \ln\left(\frac{\hbar\omega_E}{k_BT}\right).$$

When doing this type of free energy integration it is important that the two Hamiltonians in questions are not too dissimilar as this will make convergence of the method very slow. Hence, the Einstein frequency may be matched to e.g. reproduce the mean square displacement for system A for the desired temperature. For multi-component system with large mass discrepancy, such as WC, it also helps to assign different Einstein frequencies for the different components. The integration can be done via either equilibrium sampling where a few values of λ is chosen and then sampled carefully or nonequilibrium sampling where λ is changed continuously through out a simulation [65].

6

Summary of the papers

6.1 Paper I

In paper I we employ computational methods for studying the local change of the atomic structure and composition at a phase boundary. This gives rise to interfacial phases, complexions, which exists under different thermodynamic conditions. In this paper we study the phase boundary between hexagonal WC and Co and the possibility of a thin cubic WC film forming at the phase boundary. Many different stacking sequences of the cubic film is considered. The cubic WC phase favors vacancies and hence we consider the carbon lattice sites as either carbon or vacancies. This is done using cluster expansions, see Paper III, which allows for exploring the energy landscape as a function of both vacancy concentration and ordering. The configurational free energy is sampled using Monte Carlo simulations. Further, we compute the vibrational properties of the thin cubic films using harmonic force constant fitting, see Paper IV-V. This allows us to construct the interface free energies of the cubic films as function of both carbon chemical potential and temperature which allows for the interfacial phase diagram to be constructed. We predict that cubic thin films are thermodynamically stable for high temperatures and carbon chemical potentials slightly lower than obtained in the η-phases. This is in qualitative agreement with experimental observations from transmission electron microscopy studies.

6.2 Paper II

The interface energies of WC-Co cemented carbides are important to understand as they help understand and predict the microstructure of the material which is

strongly related to the mechanical properties of the material. Interface in WC-Co have been extensively studied with DFT and the ground-state 0 K interface energies have been computed. When sintering WC-Co one often reaches temperature above 1500 K for which the Co melts and thus the interface energies can change substantially.

In paper II the temperature dependency of interface free energies are studied for various different interfaces in the WC-Co system using an analytical bond order potential. This is done as a function of temperature up to and beyond the melting point of Co. We employ a few different free energy calculation methods. The calculations for the solid-liquid WC-Co interfaces proves rather challenging. To this end we employ joining simulations where the two phase (WC and Co) are initially separated and then slowly brought into contact with each other. In summary most of the interface free energies studied decreases with about 10-20% at 2000 K compared to 0 K. This provide a good complement to previous DFT calculations of interface energies.

6.3 Paper III

In paper III the ICET package is introduced. First the general formalism of alloy cluster-expansions is explained. How to construct a cluster expansion model is then discussed along with the advantages of different regression methods. The workflow and features of ICET is presented. Finally two examples, to demonstrate the usage of ICET are shown. The first one being the construction of the binary Ag-Pd FCC phase diagram via free energy sampling using Monte Carlo simulations. In the second example the chemical ordering of the inorganic clathrate $Ba_8Al_xSi_{46-x}$ is studied as a function of temperature.

6.4 Paper IV and V

In paper IV the HIPHIVE package is introduced. Detailed formalism in regards to force constants and how they can be parameterized using label symmetries, crystal symmetries and different sum rules. The workflow of and core objects in HIPHIVE is explained and finally the usage of HIPHIVE is demonstrated through two short examples. In the first example second and third order force constants are extracted for a monolayer of MoS_2. The force constants are shown to converge very quickly and for example accurate thermal conductivity can be obtained using only a few tens of structures whereas using the direct approach some hundreds would've been needed. In the second example we show how a fourth order model can be used to

account for the first anharmonic effects in dynamical properties such as the mean squared displacements.

In paper V we focus on getting a better understanding of best practices for force constant extraction using regression techniques, how sensitive thermodynamic and transport properties are with respect to the accuracy of the force constants and how to to use higher models for thermodynamic sampling.

7

Outlook

The WC-Co cemented carbide is often doped with grain growth inhibitors in order to control the grain growth rate and thus controlling the mechanical properties of the material. Typically dopants are V, Ti, and Cr which have all shown to form thin films on the surface of WC grains. These interfacial structures are most likely connected to the grain growth inhibition effect. Low dopant concentrations are used in order to avoid the precipitation of the corresponding carbide phases, but high enough to allow for the formation of the interfacial films.

The computational methods used in paper I shows promising results for the modeling of cubic films in undoped WC-Co, including carbon vacancies and vibrations. Going forward we aim to apply these methods to study the more complex systems where dopants are introduced. With additional components the configurational space quickly becomes very large. Therefore this may require some effective modeling of the vibrations as computing harmonic force constants likely become too expensive. The coupling between configurational and vibrational degrees of freedom is also an interesting topic to investigate further.

We also aim to study of the thermodynamic stability of WC hexagonal and cubic phases as a function of carbon content and temperature. This will provide a good complement to the interfacial phase diagram obtained in paper I. This will be challenging due to the anharmonic nature of the cubic phase and how the anharmonicity may change due to the introduction of carbon vacancies.

The construction of higher order force constant models can now comfortably be carried out using HIPHIVE. There are still questions on how to best sample thermodynamic and vibrational properties using higher order models. MD have been used for this and might be the best option, then the task is shifted to constructing a stable higher order model. This is something that we hopefully can investigate further in the future.

Acknowledgments

Firstly I would I like to thank my main supervisor Göran Wahnström for his support and guidance. Also thank you for pushing me to get this thesis written, it was definitely needed. I would also like to thank my co-supervisor Paul Erhart for all the inspiring discussions throughout the years.

Thank you to my office mate and good friend Mattias Ångqvist for always making the office hours entertaining in various ways.

Thank you to Martin Gren for introducing me to the cemented carbide projects, all long fruitful discussions (sorry Mattias) and for always helping me out.

Thanks to Fredrik Eriksson for making the development of HIPHIVE very enjoyable, maybe one day we'll figure out what a phonon actually is.

Thank you to current and former colleagues in the Materials and Surface Theory group for providing such a great and motivating work environment, although our type hinting practices are questionable.

Thank you to our collaborators from the SSF sintering project at KTH, Sandvik, Seco Tools and Grenoble INP.

Lastly I would like to thank my parents and sister for their support over the years, it means the world.

Bibliography

[1] H. E. Exner, *Physical and Chemical Nature of Cemented Carbides*, International Metals Reviews **24**, 149 (1979).

[2] L. Prakash, *1.02 - Fundamentals and General Applications of Hardmetals*, in *Comprehensive Hard Materials*, edited by V. K. Sarin (Elsevier, Oxford, 2014).

[3] S. Norgren, J. García, A. Blomqvist, and L. Yin, *Trends in the P/M Hard Metal Industry*, International Journal of Refractory Metals and Hard Materials **48**, 31 (2015).

[4] Z. Zak Fang and M. C. Koopman, *1.04 - Cemented Tungsten Carbide Hardmetal - An Introduction*, in *Comprehensive Hard Materials*, edited by V. K. Sarin (Elsevier, Oxford, 2014).

[5] S. Lay and J.-M. Missiaen, *1.03 - Microstructure and Morphology of Hardmetals*, in *Comprehensive Hard Materials*, edited by V. K. Sarin (Elsevier, Oxford, 2014).

[6] A. F. Guillermet, *Thermodynamic Properties of the Co-W-C System*, Metallurgical Transactions A **20**, 935 (1989).

[7] M. Christensen, G. Wahnström, C. Allibert, and S. Lay, *Quantitative Analysis of WC Grain Shape in Sintered WC-Co Cemented Carbides*, Physical Review Letters **94**, 066105 (2005).

[8] Z. Z. Fang, X. Wang, T. Ryu, K. S. Hwang, and H. Y. Sohn, *Synthesis, Sintering, and Mechanical Properties of Nanocrystalline Cemented Tungsten Carbide – A Review*, International Journal of Refractory Metals and Hard Materials **27**, 288 (2009).

[9] M. Kahlweit, *Ostwald Ripening of Precipitates*, Advances in Colloid and Interface Science **5**, 1 (1975).

[10] C. H. Allibert, *Sintering Features of Cemented Carbides WC–Co Processed from Fine Powders*, International Journal of Refractory Metals and Hard Materials **19**, 53 (2001).

[11] M. Bonvalet, J. Odqvist, J. Ågren, and A. Borgenstam, *Modelling of Prismatic Grain Growth in Cemented Carbides*, International Journal of Refractory Metals and Hard Materials **78**, 310 (2019).

[12] W. D. Schubert, A. Bock, and B. Lux, *General Aspects and Limits of Conventional Ultrafine WC Powder Manufacture and Hard Metal Production*, International Journal of Refractory Metals and Hard Materials **13**, 281 (1995).

[13] J. García, V. Collado Ciprés, A. Blomqvist, and B. Kaplan, *Cemented Carbide Microstructures: A Review*, International Journal of Refractory Metals and Hard Materials **80**, 40 (2019).

[14] M. Kawakami, O. Terada, and K. Hayashi, *HRTEM Microstructure and Segregation Amount of Dopants at WC/Co Interfaces in TiC and TaC Mono-Doped WC-Co Submicro-Grained Hardmetals*, Journal of the Japan Society of Powder and Powder Metallurgy **53**, 166 (2006).

[15] S. Lay, S. Hamar-Thibault, and M. Loubradou, *Accommodation of the Lattice Mismatch at the VCx-WC Interface*, Interface Science **12**, 187 (2004).

[16] T. Yamamoto, Y. Ikuhara, and T. Sakuma, *High Resolution Transmission Electron Microscopy Study in VC-Doped WC–Co Compound*, Science and Technology of Advanced Materials **1**, 97 (2000).

[17] S. Lay, J. Thibault, and S. Hamar-Thibault, *Structure and Role of the Interfacial Layers in VC-Rich WC-Co Cermets*, Philosophical Magazine **83**, 1175 (2003).

[18] I. Sugiyama, Y. Mizumukai, T. Taniuchi, K. Okada, F. Shirase, T. Tanase, Y. Ikuhara, and T. Yamamoto, *Formation of (W,V)Cx Layers at the WC/Co Interfaces in the VC-Doped WC–Co Cemented Carbide*, International Journal of Refractory Metals and Hard Materials **30**, 185 (2012).

[19] A. Meingast, E. Coronel, A. Blomqvist, S. Norgren, G. Wahnström, and M. Lattemann, *High Resolution STEM Investigation of Interface Layers in Cemented Carbides*, International Journal of Refractory Metals and Hard Materials **72**, 135 (2018).

[20] V. Bounhoure, S. Lay, M. Loubradou, and J.-M. Missiaen, *Special WC/Co Orientation Relationships at Basal Facets of WC Grains in WC–Co Alloys*, Journal of Materials Science **43**, 892 (2008).

[21] S. Lay, C. H. Allibert, M. Christensen, and G. Wahnström, *Morphology of WC Grains in WC–Co Alloys*, Materials Science and Engineering: A **486**, 253 (2008).

[22] X. Liu, X. Song, H. Wang, X. Liu, F. Tang, and H. Lu, *Complexions in WC-Co Cemented Carbides*, Acta Materialia **149**, 164 (2018).

[23] A. S. Kurlov and A. I. Gusev, *Tungsten Carbides and W-C Phase Diagram*, Inorganic Materials **42**, 121 (2006).

[24] S. A. E. Johansson and G. Wahnström, *A Computational Study of Thin Cubic Carbide Films in WC/Co Interfaces*, Acta Materialia **59**, 171 (2011).

[25] S. A. E. Johansson and G. Wahnström, *First-Principles Derived Complexion Diagrams for Phase Boundaries in Doped Cemented Carbides*, Current Opinion in Solid State and Materials Science **20**, 299 (2016).

[26] S. A. E. Johansson and G. Wahnström, *First-Principles Study of an Interfacial Phase Diagram in the V-Doped WC-Co System*, Physical Review B **86**, 035403 (2012).

[27] J. M. Sanchez, F. Ducastelle, and D. Gratias, *Generalized Cluster Description of Multicomponent Systems*, Physica A: Statistical Mechanics and its Applications **128**, 334 (1984).

[28] L. J. Nelson, G. L. W. Hart, F. Zhou, and V. Ozoliņš, *Compressive Sensing as a Paradigm for Building Physics Models*, Physical Review B **87**, 035125 (2013).

[29] L. J. Nelson, V. Ozoliņš, C. S. Reese, F. Zhou, and G. L. W. Hart, *Cluster Expansion Made Easy with Bayesian Compressive Sensing*, Physical Review B **88**, 155105 (2013).

[30] B. Efron, *Second Thoughts on the Bootstrap*, Statistical Science **18**, 135 (2003).

[31] K. Frisk, *A Revised Thermodynamic Description of the Ti–C System*, Calphad **27**, 367 (2003).

[32] B. Sadigh and P. Erhart, *Calculation of Excess Free Energies of Precipitates via Direct Thermodynamic Integration across Phase Boundaries*, Physical Review B **86**, 134204 (2012).

[33] A. Togo and I. Tanaka, *First Principles Phonon Calculations in Materials Science*, Scripta Materialia **108**, 1 (2015).

[34] A. Togo, L. Chaput, and I. Tanaka, *Distributions of Phonon Lifetimes in Brillouin Zones*, Physical Review B **91**, 094306 (2015).

[35] W. Li, J. Carrete, N. A. Katcho, and N. Mingo, *ShengBTE: A Solver of the Boltzmann Transport Equation for Phonons*, Computer Physics Communications **185**, 1747 (2014).

[36] J. Carrete, B. Vermeersch, A. Katre, A. van Roekeghem, T. Wang, G. K. H. Madsen, and N. Mingo, *almaBTE : A Solver of the Space–Time Dependent Boltzmann Transport Equation for Phonons in Structured Materials*, Computer Physics Communications **220**, 351 (2017).

[37] J. J. Plata, P. Nath, D. Usanmaz, J. Carrete, C. Toher, M. de Jong, M. Asta, M. Fornari, M. B. Nardelli, and S. Curtarolo, *An Efficient and Accurate Framework for Calculating Lattice Thermal Conductivity of Solids: AFLOW—AAPL Automatic Anharmonic Phonon Library*, npj Computational Materials **3**, 45 (2017).

[38] K. Esfarjani, G. Chen, and H. T. Stokes, *Heat Transport in Silicon from First-Principles Calculations*, Physical Review B **84**, 085204 (2011).

[39] F. Zhou, W. Nielson, Y. Xia, and V. Ozoliņš, *Lattice Anharmonicity and Thermal Conductivity from Compressive Sensing of First-Principles Calculations*, Physical Review Letters **113**, 185501 (2014).

[40] F. Zhou, W. Nielson, Y. Xia, and V. Ozoliņš, *Compressive sensing lattice dynamics. I. General formalism*, 2018, arXiv:1805.08903.

[41] F. Zhou, B. Sadigh, D. Åberg, Y. Xia, and V. Ozoliņš, *Compressive sensing lattice dynamics. II. Efficient phonon calculations and long-range interactions*, 2018, arXiv:1805.08904.

[42] T. Tadano and S. Tsuneyuki, *Quartic Anharmonicity of Rattlers and Its Effect on Lattice Thermal Conductivity of Clathrates from First Principles*, Physical Review Letters **120**, 105901 (2018).

[43] T. Tadano and S. Tsuneyuki, *First-Principles Lattice Dynamics Method for Strongly Anharmonic Crystals*, Journal of the Physical Society of Japan **87**, 041015 (2018).

[44] K. Esfarjani and H. T. Stokes, *Method to Extract Anharmonic Force Constants from First Principles Calculations*, Physical Review B **77**, 144112 (2008).

[45] D. C. Wallace, *Thermodynamics of Crystals* (Dover, Mineola, New York, 1998).

[46] J. Xie, S. de Gironcoli, S. Baroni, and M. Scheffler, *Temperature-Dependent Surface Relaxations of Ag(111)*, Physical Review B **59**, 970 (1999).

[47] L. T. Kong, *Phonon Dispersion Measured Directly from Molecular Dynamics Simulations*, Computer Physics Communications **182**, 2201 (2011).

[48] T. Andersson, Master's thesis, Chalmers University of Technology, Gothenburg, Sweden, 2012, *One-shot free energy calculations for crystalline materials.*

[49] O. Hellman, P. Steneteg, I. A. Abrikosov, and S. I. Simak, *Temperature Dependent Effective Potential Method for Accurate Free Energy Calculations of Solids*, Physical Review B **87**, 104111 (2013).

[50] R. W. Zwanzig, *High-Temperature Equation of State by a Perturbation Method. I. Nonpolar Gases*, The Journal of Chemical Physics **22**, 1420 (1954).

[51] T. Tadano and S. Tsuneyuki, *Self-Consistent Phonon Calculations of Lattice Dynamical Properties in Cubic* $SrTiO_3$ *with First-Principles Anharmonic Force Constants*, Physical Review B **92**, 054301 (2015).

[52] Jones J. E. and Chapman Sydney, *On the Determination of Molecular Fields. —II. From the Equation of State of a Gas*, Proceedings of the Royal Society of London. Series A, Containing Papers of a Mathematical and Physical Character **106**, 463 (1924).

[53] M. S. Daw and M. I. Baskes, *Embedded-Atom Method: Derivation and Application to Impurities, Surfaces, and Other Defects in Metals*, Physical Review B **29**, 6443 (1984).

[54] J. K. Nørskov, *Covalent Effects in the Effective-Medium Theory of Chemical Binding: Hydrogen Heats of Solution in the $3d$ Metals*, Physical Review B **26**, 2875 (1982).

[55] M. W. Finnis and J. E. Sinclair, *A Simple Empirical N-Body Potential for Transition Metals*, Philosophical Magazine A **50**, 45 (1984).

[56] G. C. Abell, *Empirical Chemical Pseudopotential Theory of Molecular and Metallic Bonding*, Physical Review B **31**, 6184 (1985).

[57] J. Tersoff, *New Empirical Approach for the Structure and Energy of Covalent Systems*, Physical Review B **37**, 6991 (1988).

[58] D. W. Brenner, *Empirical Potential for Hydrocarbons for Use in Simulating the Chemical Vapor Deposition of Diamond Films*, Physical Review B **42**, 9458 (1990).

[59] N. Juslin, P. Erhart, P. Träskelin, J. Nord, K. O. E. Henriksson, K. Nordlund, E. Salonen, and K. Albe, *Analytical Interatomic Potential for Modeling Nonequilibrium Processes in the W–C–H System*, Journal of Applied Physics **98**, 123520 (2005).

[60] M. V. G. Petisme, S. Johansson, and G. Wahnström, *Molecular Dynamics Simulations of WC/WC Grain boundary Sliding: the Effect of Thin Cobalt Films on Sliding Resistance*, Proceedings of the 18th Plansee Seminar , (2013).

[61] Frenkel, Daan and Smit, Berend, *Understanding Molecular Simulation: From Algorithms to Applications (Computational Science Series, Vol 1)* (Academic Press, San Diego, 2001).

[62] L. Verlet, *Computer "Experiments" on Classical Fluids. I. Thermodynamical Properties of Lennard-Jones Molecules*, Physical Review **159**, 98 (1967).

[63] J. G. Kirkwood, *Statistical Mechanics of Fluid Mixtures*, The Journal of Chemical Physics **3**, 300 (1935).

[64] D. Frenkel and A. J. C. Ladd, *New Monte Carlo Method to Compute the Free Energy of Arbitrary Solids. Application to the Fcc and Hcp Phases of Hard Spheres*, The Journal of Chemical Physics **81**, 3188 (1984).

[65] R. Freitas, M. Asta, and M. de Koning, *Nonequilibrium Free-Energy Calculation of Solids Using LAMMPS*, Computational Materials Science **112**, 333 (2016).